![HOKKAIDO UNIVERSITY]

Infrared-transmittance tunable metal-insulator conversion device with thin-film-transistor-type structure on a glass substrate

Takayoshi Katase, Kenji Endo, and Hiromichi Ohta

Articles you may be interested in

Thermoelectric phase diagram of the SrTiO$_3$–SrNbO$_3$ solid solution system
Journal of Applied Physics **121**, 185102 (2017); 10.1063/1.4983359

Simple ALD process for ε-Fe$_2$O$_3$ thin films
APL Materials **5**, 056104 (2017); 10.1063/1.4983038

Oxygen partial pressure dependence of surface space charge formation in donor-doped SrTiO$_3$
APL Materials **5**, 056106 (2017); 10.1063/1.4983618

Ultrafast relaxation of hot phonons in graphene-hBN heterostructures
APL Materials **5**, 056101 (2017); 10.1063/1.4982738

Effect of gate voltage polarity on the ionic liquid gating behavior of NdNiO$_3$/NdGaO$_3$ heterostructures
APL Materials **5**, 051101 (2017); 10.1063/1.4983617

Research Update: Van-der-Waals epitaxy of layered chalcogenide Sb$_2$Te$_3$ thin films grown by pulsed laser deposition
APL Materials **5**, 050701 (2017); 10.1063/1.4983403

Infrared-transmittance tunable metal-insulator conversion device with thin-film-transistor-type structure on a glass substrate

Takayoshi Katase,[1,2,a,b] Kenji Endo,[3] and Hiromichi Ohta[1,c]

[1]*Research Institute for Electronic Science, Hokkaido University, N20W10, Kita, Sapporo 001-0020, Japan*
[2]*PRESTO, Japan Science and Technology Agency, 5 Sanbancho, Chiyoda, Tokyo 102-0075, Japan*
[3]*Graduate School of Information Science and Technology, Hokkaido University, N14W19, Kita, Sapporo 060-0814, Japan*

Infrared (IR) transmittance tunable metal-insulator conversion was demonstrated on a glass substrate by using thermochromic vanadium dioxide (VO_2) as the active layer in a three-terminal thin-film-transistor-type device with water-infiltrated glass as the gate insulator. Alternative positive/negative gate-voltage applications induce the reversible protonation/deprotonation of a VO_2 channel, and two-orders of magnitude modulation of sheet-resistance and 49% modulation of IR-transmittance were simultaneously demonstrated at room temperature by the metal-insulator phase conversion of VO_2 in a non-volatile manner. The present device is operable by the room-temperature protonation in an all-solid-state structure, and thus it will provide a new gateway to future energy-saving technology as an advanced smart window. © *2017 Author(s). All article content, except where otherwise noted, is licensed under a Creative Commons Attribution (CC BY) license (http://creativecommons.org/licenses/by/4.0/).* [http://dx.doi.org/10.1063/1.4983276]

Thermochromic vanadium dioxide (VO_2) exhibits a reversible metal-insulator (MI) transition at a critical temperature (T_{MI}) of 68 °C due to the structural and electronic structure changes.[1–3] Above T_{MI}, VO_2 has a rutile-type tetragonal structure that is a metal and reflective to infrared (IR) due to the free carriers. In the low-temperature phase below T_{MI}, the V ions form a dimer, resulting in a monoclinic structure.[4] This structural transformation accompanies a dramatic change in the 3d-band configuration with appearance of charge gap ∼0.6 eV, where the VO_2 changes to be an electrical insulator and transparent to IR.[5] Thus VO_2 has the potential to demonstrate an IR-transmittance tunable MI conversion device on a glass substrate (Fig. 1), which is expected to have a significant contribution on energy saving technology as an advanced smart window, e.g., the device can selectively regulate thermal radiation from sunlight and function as an ON/OFF power switch to control the in-house temperature, which thus greatly reduces the energy consumption including light expenses and cooling/heating loads.

For the application to such a device, the control of T_{MI} in the boundary of ambient temperature is inevitable to modulate the MI transition characteristics of VO_2. Electron doping by the substitution of aliovalent metal ions, such as tungsten, at V site in VO_2 can reduce the T_{MI} down to below room temperature (RT),[6] but it is an irreversible process. The proton doping (protonation) is one of the effective ways to reversibly modulate T_{MI}; the proton can exist at an interstitial site in the VO_2 lattice and act as a shallow donor that donates an electron to a V ion,[7] similar to the electrochromic effect in H_xWO_3.[8] Compared to the state-of-the-art modulation techniques, such as electrostatic-charge

---

[a]Present address: Laboratory for Materials and Structures, Institute of Innovative Research, Tokyo Institute of Technology, 4259 Nagatsuta, Midori, Yokohama 226-8503, Japan.
[b]katase@mces.titech.ac.jp
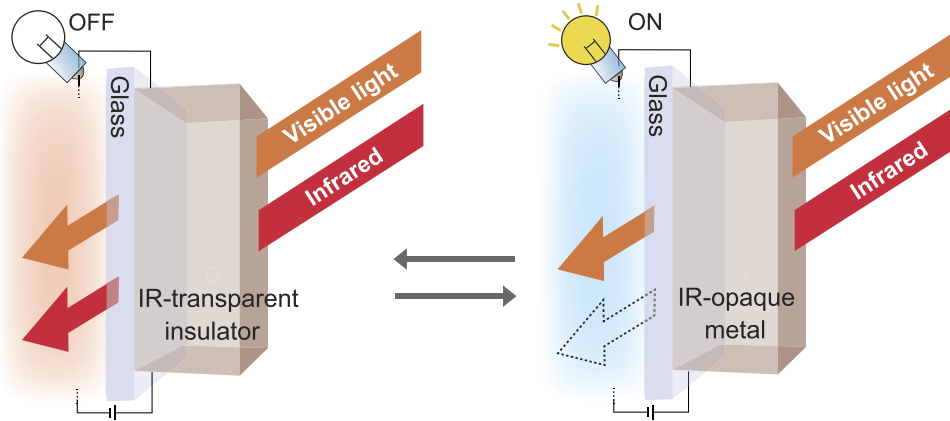[c]hiromichi.ohta@es.hokudai.ac.jp

FIG. 1. Concept of an IR-transmittance tunable MI conversion device. The device can control IR transmittance, while maintaining VIS transparency, and electrical conductivity at the same time. In the ON state (right figure), the IR cannot be transmitted through the device, whereas it can be transmitted in the OFF state (left figure), which can work as the thermal radiation control from sunlight. Further, the device can function as an ON/OFF power switch for electronic devices to control the in-house temperature. Such a device on a glass substrate would be useful as an energy-saving smart window application.

doping[9,10] and epitaxial strains in thin films,[11] the protonation of VO_2 (H_xVO_2) via a chemical route is the most ideal to switch the MI transition due to the intrinsic non-volatile operations.

However, there have been technological difficulties in the protonation of VO_2, which required a high-temperature heating with a hydrogen source.[12–14] The most appropriate route for the RT protonation is the electrochemical reaction in an electrolyte, but the uptake amount of proton (H^+) into VO_2 was too small to modulate the MI transition, where the proton insertion proceeded only to a value of $x = 0.06$ in H_xVO_2,[12] and the liquid-electrolyte likely causes a leakage problem that limits the application in practical use. Then we have recently demonstrated a new approach of water-electrolysis-induced protonation for the VO_2 epitaxial film grown on a sapphire substrate by using a three-terminal TFT-type structure with water-infiltrated nanoporous glass as a gate insulator;[15,16] this device is kind of a pseudo-solid-state electrochemical cell with a nano-gap parallel plate structure composed of a VO_2 channel and metal gate electrode, where a gate bias application induces water electrolysis in the gate insulator and the produced H^+/hydroxyl (OH^-) ion can be used to protonate/deprotonate the VO_2 channel, resulting in the reversible MI phase modulation at RT.[16] This RT-protonation approach can be realized in an all-solid-state TFT-type structure, and thus the advantageous feature should lead to a practical IR-transmittance tunable MI conversion device on a glass substrate.

Herein, we demonstrate an IR-transmittance tunable MI conversion device by extending the three-terminal TFT-type structure with a water-leakage-free gate insulator to a large-area VO_2 film prepared on a glass substrate. Figure 2(a) schematically illustrates the device structure, which has a typical three-terminal TFT geometry composed of an active VO_2 layer, a gate insulator, and source-drain-gate electrodes. The E1–E4 electrodes were used for the characterization of electronic property for the VO_2 layer. Since there have been a few papers on the MI transition characteristics of a VO_2 polycrystalline film, we have examined the material properties and examined the device characteristics using the VO_2 film on a glass substrate. The device structure with the 2.0-mm^2 VO_2 channel was fabricated on an alkaline-free glass substrate (Corning® EAGLE XG®, substrate size: $10 \times 10 \times 0.7$ mm^3) by pulsed laser deposition (PLD) using stencil masks.[17] A KrF excimer laser (wavelength of 248 nm, repetition rate of 10 Hz) was used to ablate ceramic target disks. The details of device fabrication are summarized in the supplementary material. In order to fabricate the transparent device structure, which is essential to realize IR-transmittance modulation, all the films used in this study were selected from the wide-gap oxide materials. A nickel oxide/indium tin oxide (NiO/ITO) bilayer film was used as the transparent counter/top gate electrode, and an F-doped SnO_2 film (SnO_2:F) was used as the source-drain and E1–E4 electrodes. The gate insulator consists of an amorphous $12CaO \cdot 7Al_2O_3$ thin film with a nanoporous structure (Calcium Aluminate with Nanopore, CAN);[15,18] since $12CaO \cdot 7Al_2O_3$ is a hygroscopic material, water vapor in air is automatically absorbed into the CAN film via the capillary action. Thus, a positive gate voltage (V_g) application between the
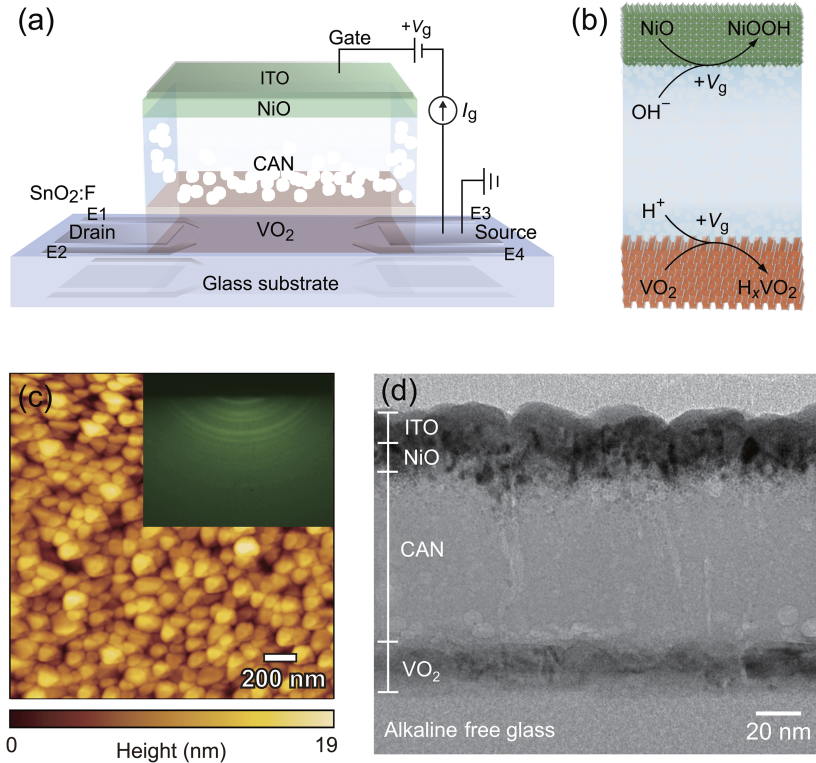
FIG. 2. (a) Schematic device structure with three-terminal transistor geometry consisting of VO_2 active layer, water-leakage-free CAN gate insulator, NiO counter layer/ITO gate electrode, and SnO_2:F source-drain electrodes, on a glass substrate. E1–E4 electrodes of SnO_2:F film were used for the electrical transport measurements. (b) Device operation mechanism. During the positive V_g application, protonation of VO_2 layer and hydroxylation of NiO layer occur simultaneously. Conversely, H_xVO_2 and NiOOH return to VO_2 and NiO during the negative V_g application. (c) Topographic AFM image of VO_2 film. RHEED pattern is superimposed in the figure, confirming the polycrystalline nature of VO_2 film. (d) Cross-sectional BF-STEM image of the device. Trilayer structure composed of VO_2 (20 nm), CAN (70 nm), and NiO (15 nm)/ITO (15 nm) layers is seen. Lighter spots in the CAN layer indicate nanopores, which is fully occupied with water.

gate and source electrodes induces electrochemical reactions such as protonation of the cathodic VO_2 layer ($VO_2 + xH^+ + xe^- \rightarrow H_xVO_2$) and hydroxylation of the anodic NiO layer (NiO + OH⁻ $\rightarrow$ NiOOH + e⁻)[19] (Fig. 2(b)). As a result, alternative positive and negative V_g applications induce the reversible protonation/deprotonation of the VO_2 channel, modulating it from IR-transparent insulator to IR-opaque metal.

Figure 2(c) shows the atomic force microscopy (AFM) image and reflection high energy electron diffraction (RHEED) pattern of the VO_2 film just deposited on a glass substrate. The film is composed of randomly oriented polycrystalline grains, which have the average grain size of 120 nm and the peak-to-valley value of 19 nm with the average surface roughness (R_a) of 2.3 nm. Figure 2(d) shows a bright-field scanning transmission electron microscopy (BF-STEM) image of the cross section of the device prepared on the VO_2 film. The each grain size of the VO_2 film was observed to be ~20 nm. Considering the average grain size in the AFM image, the VO_2 film is composed of many aggregations (with a diameter of 120 nm) of several 20-nm-size polycrystalline grains. The multi-layer structure of ITO (15 nm)/NiO (15 nm)/CAN (70 nm)/VO_2 (20 nm) was seen on a glass substrate. The crystal structure of each layer was investigated by grazing incidence X-ray diffraction analyses (data not shown), which revealed that CAN and ITO layers were amorphous in nature expect for VO_2, NiO, SnO_2:F polycrystalline layers. Lighter spots with diameters of 10–20 nm are seen in the CAN film, indicating the presence of nanopores. The device structure was designed to keep a high transmittance in both the IR and visible light region.

The conversion of electrical conductivity and IR transmittance was investigated at RT in ambient atmosphere (relative humidity value was ~30% at 25 °C). V_g was applied between the gate and

source electrodes of the device, where the drain electrode is open state and the gate current (I_g) flowing through a NiO counter electrode/CAN gate insulator/VO_2 channel layer was *in-situ* measured during the V_g application using a source measurement unit (Keithley 2450), as shown in Fig. 2(a). The opto-electronic properties were characterized immediately after each V_g application, where the sheet resistance (R_s) was measured by the DC four-probe method in the van der Pauw configuration, and optical transmittance was measured by an ultraviolet-VIS/near-IR microscope (Lamda 900s, PerkinElmer) and a Fourier-transform IR spectrometer (FT-IR 660Plus, JASCO) with the light irradiation area of 0.2×0.2 cm^2.

We first evaluated the MI-phase modulation by applying $+V_g$ (protonation). Figure 3 plots R_s of VO_2 channel as a function of applied $+V_g$, where the retention time at each $+V_g$ was set for 10 s. R_s was largely modulated from the virgin state (447 kΩ sq.$^{-1}$) by applying $+V_g$; R_s exponentially decreased and their saturation was observed at $V_g \geq +8$ V, where R_s reached to 16 kΩ sq.$^{-1}$ at +12 V. The R_s modulation should be mutually related with the flowing current in the device because of the electrochemical protonation. The inset of Fig. 3 shows the relationship between the applied $+V_g$ and accumulated sheet electron density (Q), estimated as $Q = \frac{C}{A \times q}$, where C is total coulomb amount calculated from the integral value of the I_g versus retention time during the $+V_g$ application, A is the surface area of the VO_2 channel (0.2×0.2 cm^2), and q is elementary charge, respectively. Q exponentially increased up to 1.0×10^{17} cm^{-2} ($\equiv 5.0 \times 10^{22}$ cm^{-3}) with respect to $+V_g$ and the slope becomes moderate at $V_g \geq +8$ V. The similar correlation between Q and R_s suggests that I_g flowing in the device originates from the ion current associated with the electrochemical protonation of the VO_2 channel and the critical Q of MI switching is related with the ideal Q value of 6.8×10^{16} cm^{-2} ($\equiv 3.4 \times 10^{22}$ cm^{-3}) required for the 100% protonation of a 20-nm-thick VO_2 layer, according to the following reaction: $VO_2 + H^+ + e^- \leftrightarrows HVO_2$ (Q is estimated by $Q = \frac{\rho \times t \times F}{M \times q}$, where M is the molar mass of VO_2, ρ is the film density, t is the film thickness, and F is the Faraday constant, respectively). This result suggests that almost all the provided electrons at V_g up to +8 V were used for the electrochemical protonation of the VO_2 channel, obeying Faraday's laws of electrolysis, and that the device operation can be controlled by the current density. It should be noted that Q continued to increase gradually at $V_g \geq +8$ V, while R_s was unchanged, suggesting that Q observed at $V_g \geq +8$ V originates from the gas formation by water electrolysis at the surfaces of cathodic VO_2/anodic NiO layers. The protonated H_xVO_2 channel was stable under ambient conditions at RT after the $+V_g$ application; R_s of the H_xVO_2 channel was unchanged for several days. Although it is necessary to test
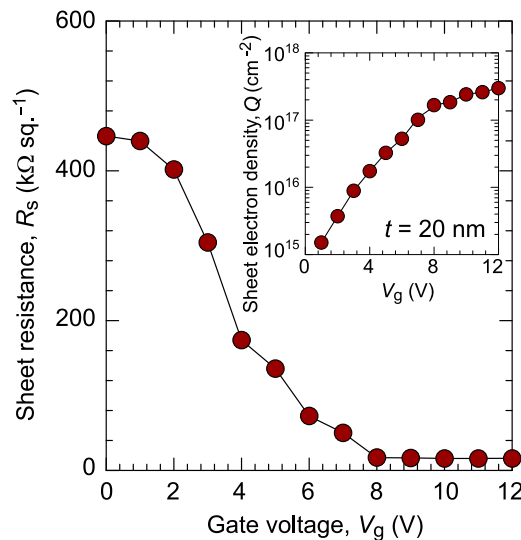

FIG. 3. Sheet resistance (R_s) as a function of V_g up to +12 V, where R_s was measured after holding the V_g application for 10 s at each step. Inset shows V_g dependence of sheet electron density (Q) accumulated during V_g application. R_s decreased with increasing V_g up to +8 V, where Q also exponentially increased with V_g due to the electrochemical protonation of VO_2 channel.
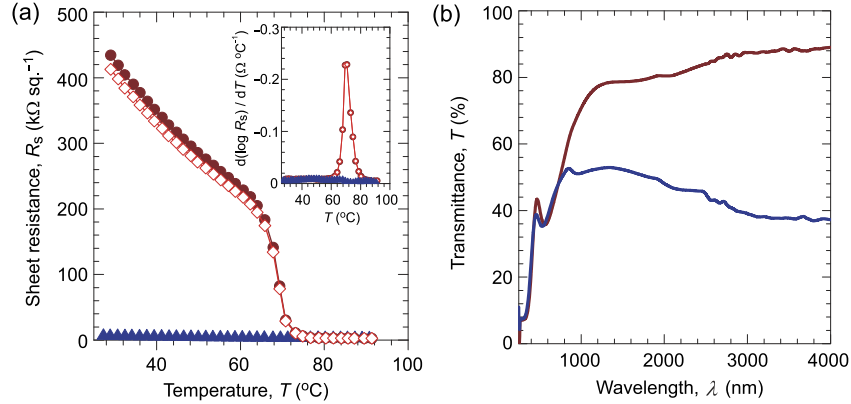
FIG. 4. (a) Temperature dependence of R_s measured before (red closed circles) and after applying V_g alternately at +12 V (protonation, blue closed triangles) and −30 V (deprotonation, red open diamond symbols). Each curve was measured after the V_g turned off, where the V_g application time was 10 s. Inset plots the temperature derivative curves of d(log R_s)/dT. (b) Optical transmittance spectra measured before (red line) and after (blue line) applying V_g = +12 V. The optical transmittance modulation ratio at λ of 3000 nm was 49%.

the retention-time dependence of R_s for the H_xVO_2 channel kept under several conditions, the result basically supports the non-volatility of device operation due to the electrochemical protonation.

Figures 4(a) and 4(b) summarize the opto-electronic properties of the device. The temperature dependence of R_s (Fig. 4(a)) was measured before and after applying V_g of +12 V (protonation) and −30 V (deprotonation) for 10 s alternately at RT in air. The R_s variation with respect to negative V_g application is shown in Fig. S1 of the supplementary material. The R_s–T curves were measured up to 90 °C during the heating runs because the deprotonation of H_xVO_2 was previously confirmed to occur at T = 100–150 °C.[16] The inset plots the temperature derivative curves of d(log R_s)/dT to clearly visualize T_{MI}. At the initial state, the MI transition was observed at T_{MI} = 70 °C, which is defined as the peak position in d(log R_s)/dT versus T, while it disappeared by applying V_g = +12 V, indicating that the VO$_2$ channel changes from an insulator to a metal at RT because of the decrease of T_{MI} below RT by the protonation. The R_s–T were reversibly modulated and recovered to initial state by applying V_g = −30 V, where two orders of magnitude modulation of R_s were observed at RT by the MI-phase conversion of VO$_2$.

It has been reported that the protonation of VO$_2$ (H_xVO_2) is thermodynamically favorable,[20] where hydrogen in VO$_2$ tends to form an strong O–H bond with the closest oxygen[12,21] and electron transfer from hydrogen onto the oxygen atom effectively reduce the electronegativity of the phase and makes it thermodynamically stable than that of pure VO$_2$ phase. Actually, deprotonation needed thermal annealing at higher temperature than that of protonation.[7] Therefore, the difference between the $+V_g$ (protonation) and $−V_g$ (deprotonation) should originate from the negative free Gibbs energy and activation barrier for the surface reaction, i.e., the in-diffusion and out-diffusion of H$^+$ transport have different interfacial resistances. Compared to the device of the VO$_2$ epitaxial film on the sapphire substrate,[16] the present device is operable by smaller DC voltage and shorter V_g application time, suggesting that the polycrystalline surface of the VO$_2$ film, shown in Fig. 2(c), enlarges the surface area with respect to that of the VO$_2$ epitaxial film and enables the effective protonation of the VO$_2$ channel layer.

Then the optical transmission spectra (Fig. 4(b)) were measured. The initial device is transparent except for the weak absorption due to the transitions between the V 3d bands with crystal-field splitting at the wavelength (λ) > 500 nm[22,23] and also due to the thin-film interference. By applying +12 V, it shows an abrupt transmittance decrease in the IR region, where the transmittance modulation ratio (ΔT) at λ = 3000 nm was 49%, while almost no change is seen in the VIS region. These results indicate that the modulation from an IR transparent insulator to an IR opaque metal was successfully demonstrated by RT protonation.

We then measured the thermopower (S) of the VO$_2$ channel protonated and deprotonated at each $\pm V_g$ in order to characterize the electronic-structure change resulting from carrier doping

(protonation).[24] Since S basically reflects the energy differential of the density of states (DOS) around the Fermi level (E_F), $\left[\frac{\partial DOS(E)}{\partial E}\right]_{E=EF}$, its value changes significantly due to the electronic-structure reconstruction across T_{MI}. S was measured at RT by giving a temperature difference (ΔT) up to ~4 K using two Peltier devices, where the actual temperatures of both sides of VO$_2$ channel layer were monitored by two tiny thermocouples with a tip diameter of 150 μm. The schematic measurement setup for thermopower was reported in Ref. 18. The thermo-electromotive force (ΔV) and ΔT were simultaneously measured, and S were obtained from the linear slope of the ΔV–ΔT plots. Figure 5(a) shows the relationship between S and $1/R_s$, where the positive V_g up to +12 V in a +1 V step was first applied for protonation and then negative V_g up to −30 V in a −3 V step was applied for deprotonation. S were always negative, indicating that the H$_x$VO$_2$ layer is an n-type conductor. The linear decrease of $|S|$ from 420 μV K^{-1} to 30 μV K^{-1} with logarithmic increase in $1/R_s$ was reversibly observed for the application of $\pm V_g$, suggesting that the protonation of the VO$_2$ channel provides electrons to the conduction band, and the energy derivative of DOS near the E_F becomes moderate, resulting in the consequent reduction of $|S|$.

Here we like to compare the present results with another electron-doping system of (V$_{1-y}$W$_y$)O$_2$ polycrystalline films grown on glass substrates. Figs. S2 and S3 of the supplementary material summarize the opto-electronic properties of (V$_{1-y}$W$_y$)O$_2$ films, where the MI transition was also modulated by W doping, and T_{MI} was suppressed below RT at $y = 0.06$ (Fig. S2). $|S|$ of (V$_{1-y}$W$_y$)O$_2$ film decreased with increasing y and became constant at small $|S|$ of 30 μV K^{-1} (Fig. S3), which is the same with the present metallic H$_x$VO$_2$ film (30 μV K^{-1}).

Lastly, in order to analyse the device operation, a simple bi-layer model of thermopower was applied to estimate the thickness (d) of metallic H$_x$VO$_2$ layer (Fig. 5(b)), where the parallel circuit composed of metal (M) and insulator (I) layers was considered to calculate the combined thermopower. Since the thermopower depends on both the conductivity and thickness of each layer, observable $|S|$ can be expressed by the equation of $|S|_{obs.} = (\sigma_{sM} \cdot |S|_M + \sigma_{sI} \cdot |S|_I)/(\sigma_{sM} + \sigma_{sI})$, where sheet conductances σ_{sM} and σ_{sI} are defined as $\sigma_M \times d$ and $\sigma_I \times (20-d)$, respectively. The physical properties of σ and $|S|$ for the I and M phases are used from those of the virgin VO$_2$ film and (V$_{1-y}$W$_y$)O$_2$ ($y = 0.06$) film, respectively. d gradually increases from the surface[25] and finally all of
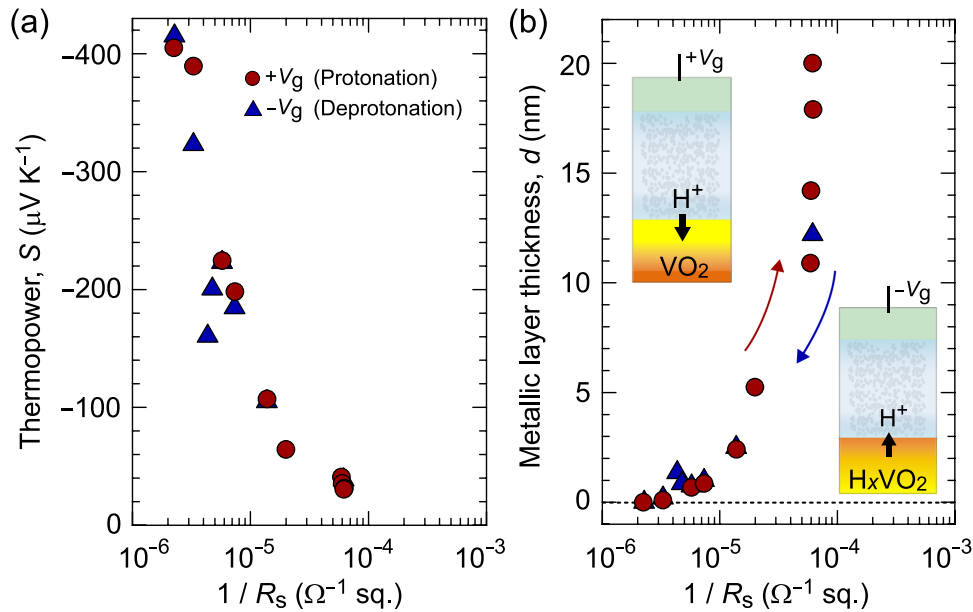

FIG. 5. Thermopower analysis of the device operation. (a) Thermopower (S) as a function of $1/R_s$ at RT by applying $+V_g$ (protonation, red circles) and $-V_g$ (deprotonation, blue triangles). The linear relation between S and logarithmic $1/R_s$ was reversibly observed by $\pm V_g$ application. (b) The thickness (d) of metallic H$_x$VO$_2$ layer with respect to $1/R_s$, estimated by thermopower analysis. d increases from the surface and finally all of the channel regions change to metallic state by applying $+V_g$. The d is reversely modulated by applying $-V_g$.

the channel regions change to a metallic state by applying $+V_g$. d reversely modulated by applying $-V_g$, indicating that the metallized H_xVO_2 film region can be controlled by applied V_g.

In summary, we have demonstrated the IR-transmittance tunable MI conversion device, which has a three-terminal TFT geometry consisting of transparent oxide thin films of VO_2 active channel, water-leakage-free CAN gate insulator, NiO counter layer/ITO gate electrode, and SnO_2:F source-drain electrodes, on a glass substrate. At initial state, the device was an insulator and transparent in the IR region. For $+V_g$ application, R_s decreased due to the protonation of the VO_2 channel and the device became IR opaque state. For $-V_g$ application, the deprotonation of the H_xVO_2 channel occurred and the device returned to the insulator/IR transparent state. The two orders of magnitude modulation of R_s and 49% modulation of IR transmittance at λ of 3000 nm were simultaneously demonstrated at RT by the metal-insulator phase conversion of VO_2 in a non-volatile manner.

The present IR-transmittance tunable MI conversion device has several advantages. The device can be fabricated on a glass substrate, which is suitable for the application to a glass window; the device fully transmits IR in the OFF state, whereas it does not transmit in the ON state. Meanwhile, the device can function as an ON/OFF power switch for electronic devices to control the in-house temperature. Moreover, the device can be operated by RT-protonation without sealing thanks to the water-leakage-free CAN gate insulator; the all-solid-state structure can resolve the liquid-leakage problem, which is a beneficial point compared to the liquid-electrolyte gated devices.[26] Although the demonstration of power saving by this device should be necessary to show the suitability for the practical application, the present device concept provides a potential gateway to a new functional device for future energy saving technologies such as advanced smart windows.

See supplementary material for device fabrication and sample preparation for transmission electron microscopy, discussion on device operation mechanism and the protonation of the VO_2 channel layer, and Figs. S1–S3.

[1] F. J. Morin, Phys. Rev. Lett. **3**, 34 (1959).
[2] C. N. Berglund and H. J. Guggenheim, Phys. Rev. **185**, 1022 (1969).
[3] J. B. Goodenough, J. Solid State Chem. **3**, 490 (1971).
[4] M. Marezio, D. B. McWhan, J. P. Remeika, and P. D. Dernier, Phys. Rev. B **5**, 2541 (1972).
[5] M. M. Qazilbash, M. Brehm, B.-G. Chae, P.-C. Ho, G. O. Andreev, B.-J. Kim, S. J. Yun, A. V. Balatsky, M. B. Maple, F. Keilmann, H.-T. Kim, and D. N. Basov, Science **318**, 1750 (2007).
[6] K. Shibuya, M. Kawasaki, and Y. Tokura, Appl. Phys. Lett. **96**, 022102 (2010).
[7] J. Wei, H. Ji, W. Guo, A. H. Nevidomskyy, and D. Natelson, Nat. Nanotechnol. **7**, 357 (2012).
[8] C. G. Granqvist, Sol. Energy Mater. Sol. Cells **92**, 203 (2008).
[9] M. Nakano, K. Shibuya, D. Okuyama, T. Hatano, S. Ono, M. Kawasaki, Y. Iwasa, and Y. Tokura, Nature **487**, 459 (2012).
[10] J. Jeong, N. Aetukuri, T. Graf, T. D. Schladt, M. G. Samant, and S. S. P. Parkin, Science **339**, 1402 (2013).
[11] T. Nan, M. Liu, W. Ren, Z.-G. Ye, and N. X. Sun, Sci. Rep. **4**, 5931 (2014).
[12] A. M. Chippindale, P. G. Dickens, and A. V. Powell, J. Solid State Chem. **93**, 526 (1991).
[13] V. N. Andreev, V. M. Kapralova, and V. A. Klimov, Phys. Solid State **49**, 2318 (2007).
[14] C. Wu, F. Feng, J. Feng, J. Dai, L. Peng, J. Zhao, J. Yang, C. Si, Z. Wu, and Y. Xie, J. Am. Chem. Soc. **133**, 13798 (2011).
[15] H. Ohta, Y. Sato, T. Kato, S. W. Kim, K. Nomura, Y. Ikuhara, and H. Hosono, Nat. Commun. **1**, 118 (2010).
[16] T. Katase, K. Endo, T. Tohei, Y. Ikuhara, and H. Ohta, Adv. Electron. Mater. **1**, 1500063 (2015).
[17] T. Katase, K. Endo, and H. Ohta, Phys. Rev. B **92**, 035302 (2015).
[18] H. Ohta, T. Mizuno, S. Zheng, T. Kato, Y. Ikuhara, K. Abe, H. Kumomi, K. Nomura, and H. Hosono, Adv. Mater. **24**, 740 (2012).
[19] X. H. Xia, J. P. Tu, J. Zhang, X. L. Wang, W. K. Zhang, and H. Huang, Sol. Energy Mater. Sol. Cells **92**, 628 (2008).
[20] A. M. Chippindale and P. G. Dickens, J. Mater. Chem. **2**, 601 (1992).
[21] Y. Filinchuk, N. A. Tumanov, V. Ban, H. Ji, J. Wei, M. W. Swift, A. H. Nevidomskyy, and D. Natelson, J. Am. Chem. Soc. **136**, 8100 (2014).
[22] H. W. Verleur, A. S. Barker, Jr., and C. N. Berglund, Phys. Rev. **172**, 788 (1968).
[23] A. Gavini and C. C. Y. Kwan, Phys. Rev. B **5**, 3138 (1972).
[24] T. Katase, K. Endo, and H. Ohta, Phys. Rev. B **90**, 161105 (2014).
[25] T. Sasaki, H. Ueda, T. Kanki, and H. Tanaka, Sci. Rep. **5**, 17080 (2015).
[26] M. Nakano, K. Shibuya, N. Ogawa, T. Hatano, M. Kawasaki, Y. Iwasa, and Y. Tokura, Appl. Phys. Lett. **103**, 153503 (2013).